Journal of Power Sources, 49 (1994) 257–270

The kinetics of electrochemical reactions on high temperature fuel cell electrodes

J. Divisek[a], L.G.J. de Haart[a], P. Holtappels[a], T. Lennartz[a], W. Malléner[b], U. Stimming[a] and K. Wippermann[a,*]

[a]*Institute of Energy Process Engineering (IEV),* [b]*Institute of Materials for Energy Technology (IWE), Research Centre Jülich (KFA), 52425 Jülich (Germany)*

Abstract

The rates of electrochemical reactions relevant for use in high-temperature solid oxide fuel cells (SOFC) has been investigated as a function of electrode potential, temperature and composition of the gas mixture. From Arrhenius plots, apparent activation energies, E_a, and apparent pre-exponential factors, A, were calculated for the oxygen-reduction and oxygen-evolution reactions at $La_{0.84}Sr_{0.16}MnO_3$ cathodes. At low overpotentials ($|\eta| \leqslant 0.2$ V), both apparent activation energies and apparent pre-exponential factors are much higher in the temperature range $T = 800$–1000 °C ($E_a \approx 160$–210 kJ/mol, $\log A \approx 6$–9) compared with those in the range $T = 500$–800 °C ($E_a \approx 80$–110 kJ/mol, $\log A \approx 2$–4). For oxygen reduction, reaction orders of $z_e = 1$ at $p_{O_2} > 0.2$ bar and $z_e = 0.5$ at $p_{O_2} < 0.2$ bar were obtained. These values may be related to either oxygen adsorbed as molecules or atoms as the reacting species. From impedance spectroscopy, it follows that the rate of the oxygen-exchange reaction is determined not only by charge transfer, but also by another process, possibly the adsorption or surface diffusion of intermediates. For the nickel zirconia cermet anode fabricated by wet powder spraying (WPS), an increase in sintering temperature to 1400 °C results in an increase in current density. A current density of 0.27 A cm^{-2} at an overvoltage of 0.1 V may be achieved. From Arrhenius plots, an energy of activation of 130 ± 10 kJ mol^{-1} was determined.

Introduction

When investigating the electrochemical behaviour of high-temperature fuel cell electrodes, it is important to vary both temperature and gas partial pressure in addition to the electrode potential. This allows one to obtain fundamental information concerning the reaction mechanisms of oxygen reduction, oxygen evolution, hydrogen oxidation and hydrogen evolution. In addition, due to temperature and pressure gradients in the fuel cell stack, the dependence of the current density on these parameters must be known. An important goal in the development of solid oxide fuel cells (SOFC) systems is to lower the average temperature in the stack. In order to systematically develop electrode materials with a high catalytic activity at lower temperatures (700 or 800 °C), it is necessary to investigate electrode kinetics in a broad temperature range in the first place.

In addition to the parameters of temperature and oxygen partial pressure, the geometry and chemical composition of the reaction zone, i.e., the so-called 'triple contact zone', has a strong influence on the rate constant of the electrochemical reactions. Hence, fabrication parameters such as sintering temperature, which determine

*Author to whom correspondence should be addressed.

SSDI 0378-7753(93)01817-2

the morphology and chemical composition of the electrodes, are of great importance. Such effects are described in this paper.

Experimental

Preparation of the electrodes

The electrodes were prepared by wet powder spraying (WPS), a new technique for the production of porous ceramic or metallic layers [1]. Using a mask, cathode discs with a diameter of 10 mm were sprayed on the electrolyte disc, which was composed of 8 mol% yttria-stabilized ZrO_2 (Tosoh TZ-8Y powder, fabricated by tape casting) and had a thickness of about 130 μm and a diameter of 19.5 mm. The $La_{0.84}Sr_{0.16}MnO_3$ cathodes investigated in this paper had a strontium content of $x=0.16$, a thickness of about 50 μm and a porosity of about 30%.

Oxidation of hydrogen was investigated at Ni–YSZ cermet layers (50 vol.% Ni; 50–80 μm thick; 0.5 cm^2 geometrical surface area) deposited on YSZ electrolyte foils (120–200 μm thick) by the WPS technique.

Cell design

A schematic sketch of the cell geometry, using a cell for cathode studies as an example, is shown in Fig. 1. The counter electrode, which was painted on the electrolyte using platinum paste (Demetron 308A), had a diameter of 8 mm. This geometry partially compensates the ohmic drop in the electrolyte, because the potential difference between the equipotential lines at the reference electrode and at the working electrode is reduced, due to edge effects. This result was obtained by a mathematical study of the current and potential distribution in the electrolyte by varying the ratio of the diameter of the working electrode to that of the counter electrode. It is particularly evident for thin electrolytes. A detailed description of the method of calculation will be described elsewhere [2]. The reference electrode was a platinum paste ring.

Different oxygen partial pressures were obtained by appropriately mixing either air and argon or oxygen and argon. Most measurements were carried out under symmetrical conditions, with the oxygen partial pressure identical on both sides of the

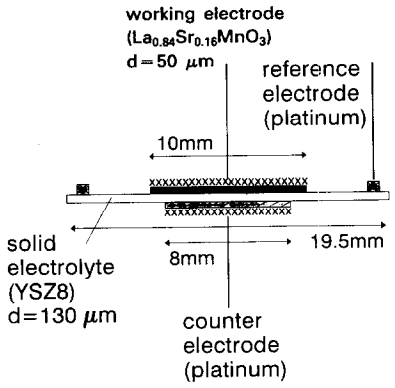

Fig. 1. Schematic view of the cross section of the measuring cell.

electrolyte. Only when low oxygen partial pressures were studied at the cathode air was supplied to the counter electrode. In this case, a gold seal was used to separate the working electrode and the counter electrode chambers.

Hydrogen oxidation at nickel–zirconia cermets was investigated in a gas stream containing hydrogen, water vapour, argon and small amounts of oxygen. The fuel gas composition was controlled by mass-flow controllers for hydrogen and argon and a water container with controlled water partial pressure. The hydrogen/water vapour ratio results in an oxygen partial pressure which is determined by the thermodynamic water equilibrium. For 1273 K and a hydrogen partial pressure of 0.18×10^5 Pa with a hydrogen/water vapour ratio of 2/1, the oxygen partial pressure amounts to 6.5×10^{-11} Pa. The oxygen partial pressure depends on the temperature, and can be calculated from the temperature dependence of the equilibrium constant.

Electrochemical apparatus

With the three-electrode cell described above, both potentiodynamic current–potential measurements and impedance measurements were performed using a Solartron 1286 electrochemical interface or a PAR 273 potentiostat and a Solartron 1255 frequency response analyser. The a.c. signal voltage was always ± 10 mV r.m.s. The impedance measurements were analysed with the 'equivalent circuit' computer code [3]. A correction of the current–potential curves for ohmic resistances was not necessary because the ohmic loss in the electrolyte was eliminated by the cell geometry described above. Other ohmic losses, such as contact resistances, were negligible.

Results and discussion

Oxygen electrode

The influence of temperature

Tafel plots (semilogarithmic plots of the current density j versus overpotential η) for oxygen reduction and oxygen evolution on $La_{0.84}Sr_{0.16}MnO_3$ cathodes at different temperatures were obtained from potentiodynamic current–potential curves (Fig. 2). All measurements were carried out under air atmosphere. At low overpotentials, approximately straight lines with small b factors (reciprocal slope of the log j/η plot)

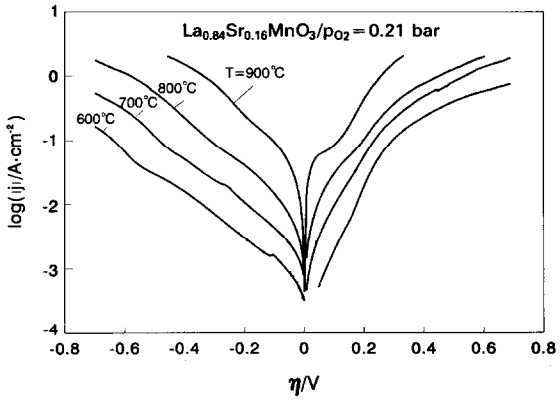

Fig. 2. Tafel plots for oxygen reduction and oxygen evolution on $La_{0.84}Sr_{0.16}MnO_3$ cathodes; $T = 600$, 700, 800 and 900 °C; $p_{O_2} = 0.21$ bar; data obtained from potentiodynamic current–potential measurements, $dE/dt = 1.7$ mV s^{-1}.

were obtained, while b factors were larger at high overpotentials. In general, the cathodic and anodic branches of the Tafel plots exhibited an asymmetric behaviour with different b factors and different exchange-current densities. For example at $T=600$ °C and low overpotentials, $b_-=-126$ mV, $b_+=46$ mV, $i_{0,-}=-0.6$ mA cm^{-2} and $i_{0,+}=0.2$ mA cm^{-2}. Unexpectedly, the Tafel slope does not change with the temperature in the usual way, which assumes that increasing overpotential lowers activation energy, thus exponentially increasing the current density. For example, at low cathodic overpotential, b_- decreases from -126 mV ($T=600$ °C) to -92 mV ($T=900$ °C), which contradicts the expectation that the b factor should linearly increase with temperature.

More detailed information about the temperature dependence of the current density is obtained from Arrhenius plots, which have been calculated for different cathodic and anodic overpotentials (Fig. 3). From the slope of the intercept of the Arrhenius plots at $1/T=0$, apparent activation energies and apparent pre-exponential factors as a function of the overpotential were calculated. An interesting feature of the Arrhenius plots at low cathodic and anodic overpotentials is the existence of two temperature regimes with different activation energies. In the temperature range $T<800$ °C, the activation energy (E_a) is ≈ 100 kJ mol^{-1}, while at higher temperatures $T>800$ °C, E_a is ≈ 200 kJ mol^{-1}. The potential dependencies of A and E_a are considerably different in the two temperature regimes (as shown in Figs. 4(a, b)). In the high temperature range (Fig. 4(a)), oxygen reduction curves and oxygen evolution curves are similar. Two ranges of overpotentials are observed, where the logarithms of A and E_a change linearly with η. In addition, the shapes of the log A versus η and E_a versus η curves are similar, with maxima at $\eta=-0.25$ V and $\eta=0.2$ V, respectively. The increase of E_a with overpotential at $|\eta|<|\eta_{max}|$ is contrary to the expectation, i.e., that the activation energy should decrease with increasing overpotential. However, the current density still increases exponentially with overpotential, due to an even larger increase in the pre-exponential factor with overpotential. At higher overpotentials ($|\eta|>|\eta_{max}|$), E_a decreases strongly with overpotential, and is compensated by a parallel decrease in A. In the lower temperature regime ($T<800$ °C, Fig. 4(b)), the shape and symmetry of the curves change notably. For this case, the curves for

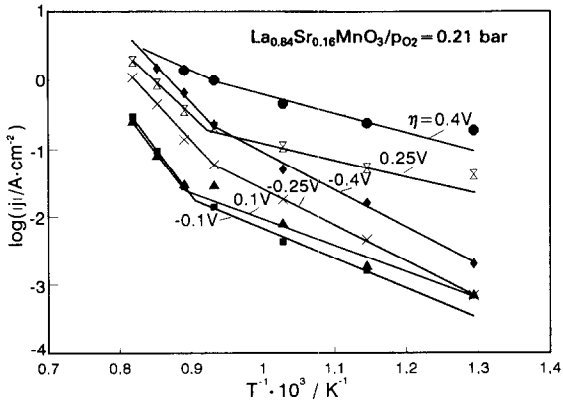

Fig. 3. Arrhenius plots calculated from current–potential curves in the temperature range from 500–1000 °C, $\eta=-0.1$, -0.25, -0.4, 0.1, 0.25 and 0.4 V.

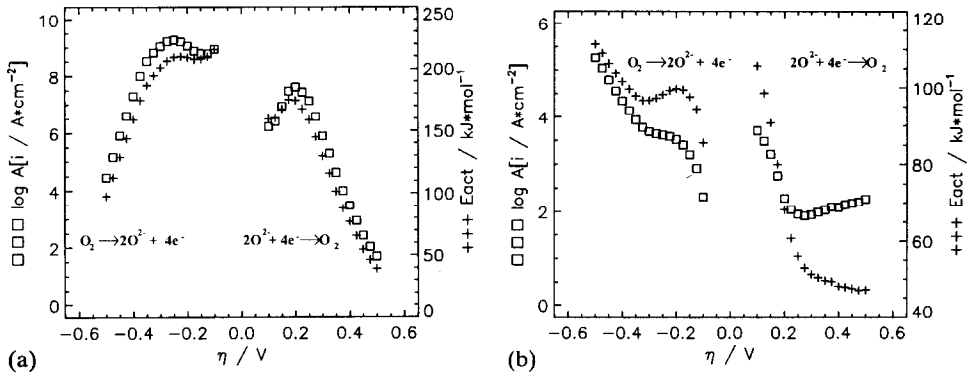

Fig. 4. (a) Activation energy, E_a, and pre-exponential factor, A, as a function of overpotential, η. Values were obtained from Arrhenius plots in the potential range of $-0.5\ V < \eta < 0.5\ V$ and the temperature range of $800\ °C \leqslant T \leqslant 1000\ °C$. (b) Activation energy, E_a, and pre-exponential factor, A, as a function of overpotential, η. Values obtained from Arrhenius plots in a potential range of $-0.5\ V < \eta < 0.5\ V$ and a temperature range of $500\ °C \leqslant T \leqslant 800\ °C$.

oxygen reduction and oxygen evolution are different, with both positive and negative slopes. Minima and inflexions are observed in the curves, at a cathodic overpotential $\eta = -0.32$ V and an anodic overpotential of $\eta = 0.27$ V. The slopes of all curves of Fig. 4 are summarized in Table 1. The strong potential dependence of the activation energy is striking; most of the slopes are close to multiple integers of the Faraday constant, F, e.g., 1, 3, 4, or 6 F. If a charge-transfer reaction is rate determining, $dE_a/d\eta$ equals $\alpha_+ nF$ and $\alpha_- nF$, respectively, where α is the transfer coefficient, whose value depends on the reaction mechanism. The product of the number of transferred electrons, n, and the transfer coefficient (α_+ or α_-) are thus an integer value. A negative dependence of the activation energy on overpotential and thus an apparent negative transfer coefficient cannot be explained by the usual theory of charge transfer. Furthermore, the dependence of the pre-exponential factor on overpotential is not yet understood, and may be due to a complex reaction scheme. In general, common charge-transfer theory requires the pre-exponential factor to be largely independent of overpotential.

The influence of oxygen partial pressure

The dependence of the oxygen partial pressure on current density was investigated in a range of $p_{O_2} = 0.01$–1 bar. Figure 5 shows Tafel plots of oxygen reduction and oxygen evolution obtained at different oxygen partial pressures at a temperature of $T = 1000$ °C. As the equilibrium potential is dependent on the oxygen partial pressure, the logarithm of current density is plotted as a function of the electrode potential, with the equilibrium potential of the air electrode used as a reference. The anodic branches of the Tafel plots are coincident, while the cathodic current increases with increasing oxygen partial pressure. From a double logarithmic plot of j versus p_{O_2} (Fig. 6), electrochemical reaction orders (z_e) of the cathodic and anodic partial reactions can be calculated. From Fig. 6, a reaction order of 0 for oxygen evolution is obtained. This is due to almost constant concentration of the oxygen ions and the oxygen ion vacancies in the electrolyte for a wide range of oxygen partial pressures. For oxygen reduction, two different electrochemical reaction orders ($z_e = 0.5$ at lower oxygen partial pressures ($p_{O_2} < 0.2$ bar) and $z_e = 1$ at $p_{O_2} > 0.2$ bar) are obtained. These values (0.5 and 1) are electrochemical reaction orders at constant potential. According to Vetter

TABLE 1

Slopes of the plots log A/E_a vs. η, data calculated from Figs. 4(a, b)

	800 °C $\leqslant T \leqslant$ 1000 °C				500 °C $\leqslant T \leqslant$ 800 °C			
	$\lvert\eta\rvert < -0.25$ V	$\lvert\eta\rvert > -0.25$ V	$\eta < 0.2$ V	$\eta > 0.2$ V	$\lvert\eta\rvert < -0.32$ V	$\lvert\eta\rvert > -0.32$ V	$\eta < 0.27$ V	$\eta > 0.27$ V
$(dE_a/d\eta)$ (eV/V)	−0.5	6.1	2.9	−5.9	0.5	−1.1	−3.9	−0.3
(d log $A/d\eta$) (V^{-1})	−5.4	28	24	−25	−1.2	−8.8	−30	1.5

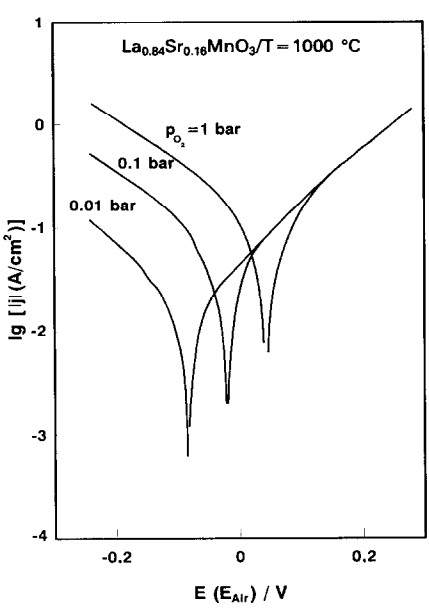

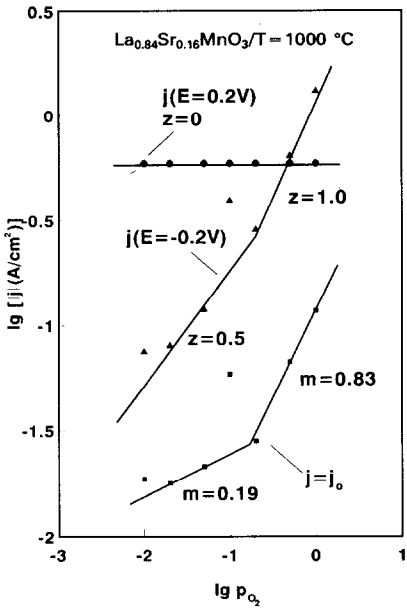

Fig. 5. Tafel plots for oxygen reduction and oxygen evolution at different oxygen partial pressures, $p_{O_2}=0.01$, 0.1 and 1 bar; $T=1000$ °C.

Fig. 6. Double logarithmic plot of the current density vs. oxygen partial pressures at $\eta=0$ and $\eta=-0.2$ V; $T=1000$ °C.

[4, 5], the chemical formula of the reduced species involved in the charge-transfer reaction of the oxygen electrode can be obtained by using the equations:

$$z_{e,O_2}=1 \quad S_r=0V_O^{\cdot\cdot}+1O_{2,ad}=O_{2,ad} \tag{1}$$

$$z_{e,O_2}=0.5 \quad S_r=0V_O^{\cdot\cdot}+0.5O_{2,ad}=O_{ad} \tag{2}$$

where S_r is the chemical formula of the reduced species, and $V_O^{\cdot\cdot}$ the oxygen ion vacancy in the solid electrolyte (Kröger–Vink notation).

Hence, at high oxygen partial pressures, molecular oxygen reacts in the charge-transfer reaction, while at lower p_{O_2}, atomic oxygen appears to be involved. Therefore, at a typical oxygen partial pressure of 0.2 bar, both molecular and atomic adsorbed oxygen are present. Furthermore, a plot of the logarithm of the exchange-current density ($\log j_0$) versus $\log p_{O_2}$ shows a slope (m) of 0.83 at high oxygen partial pressures and 0.19 at low oxygen partial pressures, i.e., the exchange-current density depends on the oxygen partial pressure according to $j_0 \sim (p_{O_2})^m$ [6]. A simple calculation of m is only possible if several assumptions are obeyed:

(i) only one reaction step is rate determining, this requires that the same reaction step is rate determining for the cathodic as well as the anodic partial reaction;

(ii) oxygen adsorption may be described by a Langmuir isotherm;

(iii) oxygen is adsorbed as molecules or atoms;

(iv) the surface coverage is either small ($\theta \ll 1$) or large ($\theta \approx 1$).

A quantitative correlation of the exponents obtained in this study under these limiting conditions was not possible. Qualitatively, the high slope of $m=0.83$ indicates molecular adsorption and the small slope of $m=0.19$ may refer to dissociative adsorption,

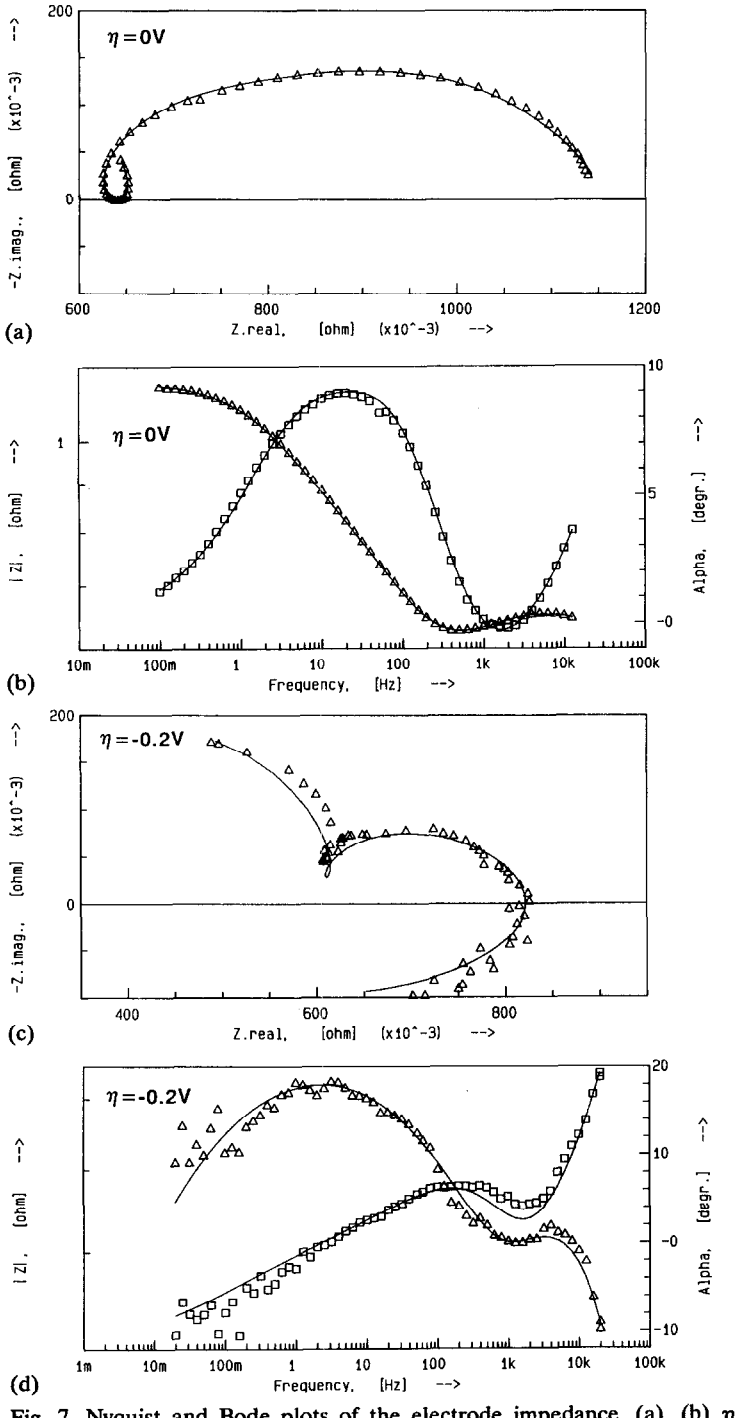

Fig. 7. Nyquist and Bode plots of the electrode impedance, (a), (b) $\eta=0$, and (c), (d) -0.2 V, $p_{O_2}=0.21$ bar; $T=1000$ °C; frequency, $f=0.1$ Hz–20 kHz; (□)/(△) measured values, (——) fit curves.

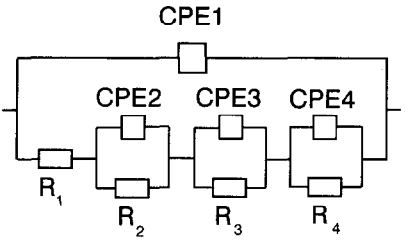

Fig. 8. Equivalent circuit used for the fit of the impedance data.

TABLE 2

Values of the equivalent circuit parameters obtained by fitting the electrode impedance shown in Fig. 7

η/V	CPE ($s^n\ \Omega^{-1}$) (n)				R (Ω)			
	1	2	3	4	1	2	3	4
0	5.5×10^{-6} (1.00)	1.1×10^{3} (−0.66)	5.7×10^{-2} (0.76)	3.1×10^{-1} (0.69)	5.9×10^{-1}	2.3×10^{-1}	3.6×10^{-1}	5.8×10^{-2}
−0.2	1.8×10^{-5} (1.00)	1.5×10^{4} (−0.86)	3.6×10^{-2} (0.80)	5.2×10^{-1} (−0.53)	3.0×10^{-1}	2.1×10^{-1}	2.2×10^{-1}	4.6×10^{-1}

which is in agreement with the chemical reaction orders obtained. Furthermore, the positive sign of the slopes suggests that there is a small coverage of adsorbed oxygen species.

Impedance spectroscopy

Additional information is obtained from impedance spectroscopy. Figure 7 shows Nyquist plots and Bode plots of the electrode impedance in the frequency range 10^{-1}–10^{4} Hz at the equilibrium potential ($\eta=0$ V, Figs. 7(a, b)) and at a cathodic overpotential ($\eta=-0.2$ V, Figs. 7(c, d)). The measured values, indicated by triangles or squares, are compared with fitted data represented by solid lines. In the Nyquist plots, at least four depressed semi-arcs may be identified, corresponding to capacitive and inductive loops. Following Van Hassel *et al.* [7], the best computer data fit is obtained using the equivalent circuit shown in Fig. 8. This consists of constant phase element CPE1 in parallel with a resistance R1, and a series of parallel combinations of three resistances (R1–R4) and constant phase elements (CPE2–CPE4). While resistance R1 is assumed to be the charge-transfer resistance (R_{ct}), the CPE1 at high frequency is interpreted as the double-layer capacitance C_{dl}. The other constant phase elements at lower frequencies can be associated with the presence of adsorbed oxygen species such as O_{ad}, $O_{2,ad}$ or O_{ad}^{-}. As Van Hassel *et al.* [7] have indicated, inductive loops can be related to stepwise transfer of electrons to adsorbed intermediates. The values of the circuit elements calculated for different cathodic overpotentials are listed in Table 2. Because the value of the charge-transfer resistance ($R1\equiv R_{ct}=0.59\ \Omega$ at $\eta=0$ V and $R_{ct}=0.3\ \Omega$ at $\eta=-0.2$ V) is in the same range as the sum of the resistances R2–R4, the rate of the oxygen-exchange reaction is determined not only by charge transfer but also by another process, such as adsorption or surface diffusion

of intermediates. The CPE1 increases from about 10 μF cm^{-2}, at the equilibrium potential, to $\approx$40 μF cm^{-2} at $\eta = -0.2$ V. The latter result agrees with results obtained from impedance measurements with blocking gold electrodes on YSZ single crystals [8], and can be related to the space-charge capacity in the electrolyte.

Influence of sintering temperature

The sintering temperature T_s has an important influence on the electrode performance. Figure 9 shows Tafel plots for oxygen reduction at three different sintering temperatures. The influence of sintering temperature T_s is remarkable. By decreasing T_s from 1500 to 1200 °C, the current density increases by five orders of magnitude. A tentative explanation of this result can be deduced from the scanning electron micrographs of the interface electrode/electrolyte cross sections (Fig. 10). After sintering, the average diameter of the contact points between the electrode and the electrolyte increases from about 0.1 μm at $T_s = 1200$ °C to 5 μm at $T_s = 1500$ °C. In parallel, the length of the reaction zone per unit area decreases from 2×10^5 cm^{-1} to 2×10^3 cm^{-1}. The latter values are calculated from Fig. 10 assuming spherical cross sections of the contact points. If the current is normalized to the length of the reaction zone (L_{tcz}), as shown in Fig. 11, the current densities for sintering temperatures of 1200 and 1300 °C differ only by a factor of three, whereas the current density at a sintering temperature of 1500 °C remains 2 to 3 orders of magnitude lower. The latter cannot be explained by a simple geometric effect. It is rather due to a diminished catalytic

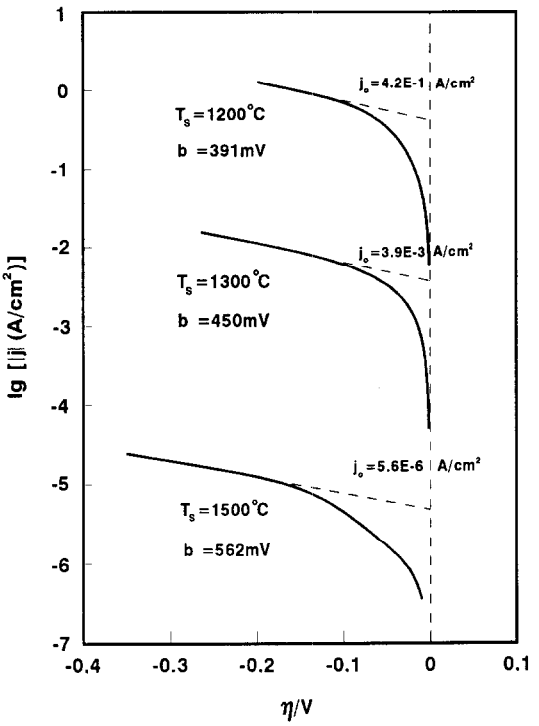

Fig. 9. Tafel plots for oxygen reduction at different sintering temperatures, $T_s = 1200$, 1300 and 1500 °C; $La_{0.84}Sr_{0.16}MnO_3$; $p_{O_2} = 0.21$ bar; $T = 1000$ °C.

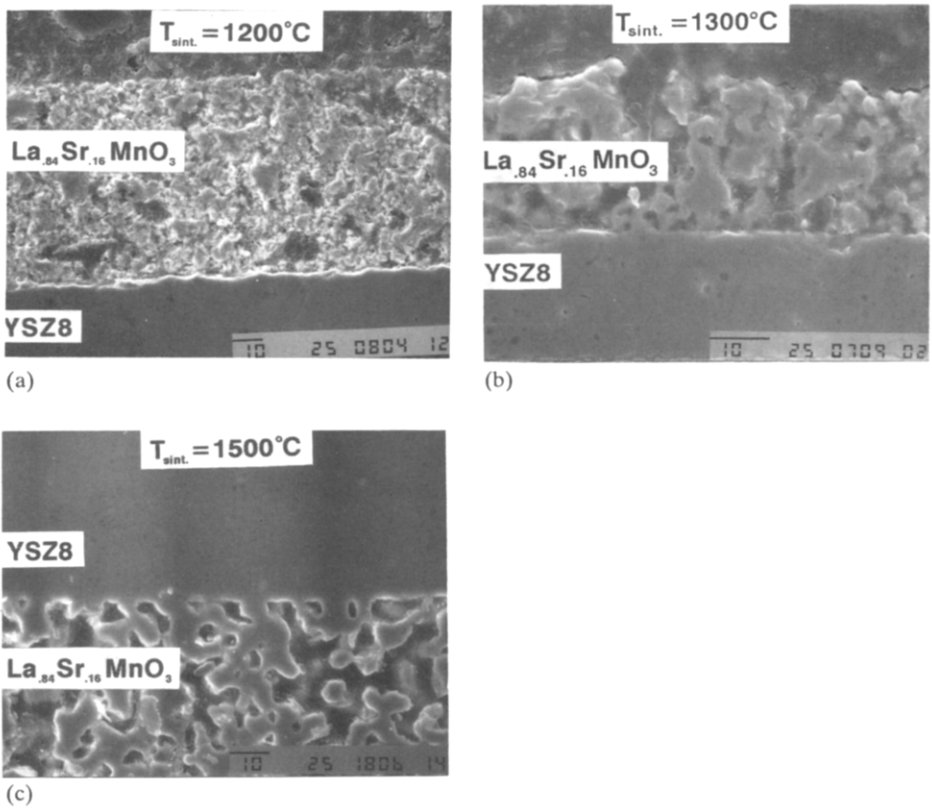

Fig. 10. Scanning electron micrographs of cross sections of the cathode/electrolyte interface, T_s= (a) 1200 °C; (b) 1300 °C, and (c) 1500 °C.

activity of the electrode material, resulting from the formation of electronically insulating phases such as $La_2Zr_2O_7$. $La_2Zr_2O_7$ has a low specific conductivity of $\sigma = 3 \times 10^{-4}$ S cm^{-1} at $T = 1000$ °C, assuming oxygen ions to be the charge carriers [9]. An interesting feature of the Tafel plots is the increase of the Tafel factor b with increasing sintering temperature. This result cannot be explained by a geometric effect, because the b factor should be independent of the length of the reaction zone. Hence, the formation of electronically insulating layers with a small specific conductivity may be responsible for the variation of b. This is supported by a large difference in the b factors: at $T_s = 1300$ °C b_- has a value of 450 mV (1.78 RT/F) and at $T_s = 1500$ °C b_- is 562 mV (2.23 RT/F). The reaction lengths in the triple contact zone at $T_s = 1300$ °C ($L_{tcz} = 6 \times 10^3$ cm^{-1}) and $T_s = 1500$ °C ($L_{tcz} = 2 \times 10^3$ cm^{-1}), however, have the same order of magnitude. A correlation of the b factors with a given reaction mechanism is not possible. At high sintering temperatures, a change in reaction mechanism may occur, because charge transfer may take place at the electrode/insulating layer interface instead of the electrode/electrolyte interface.

Hydrogen electrode

Figure 12 shows the steady-state current-density/overvoltage curves recorded for a Ni–YSZ cermet with $H_2/H_2O = 2/1$ in argon at different temperatures. Impedance

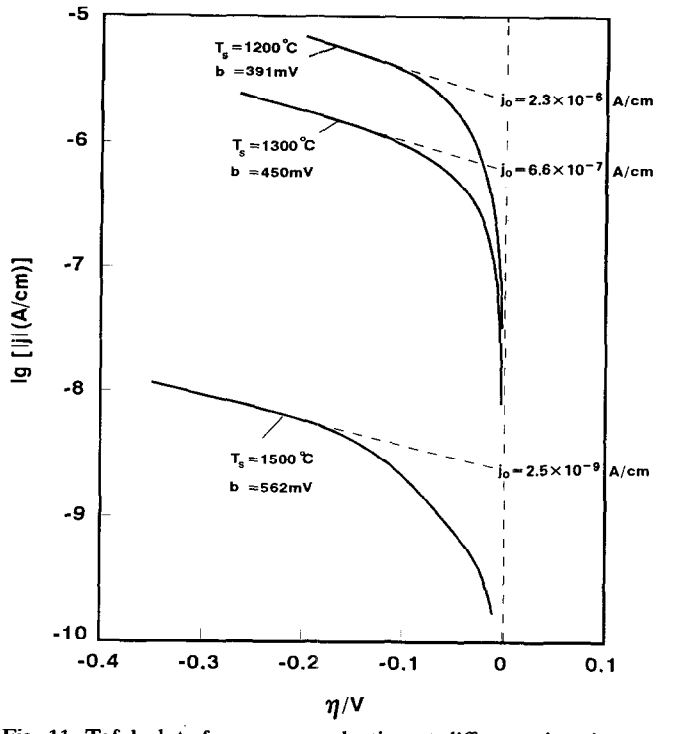

Fig. 11. Tafel plots for oxygen reduction at different sintering temperatures $T_s = 1200$, 1300 and 1500 °C. Current normalized to the length of the reaction zone and calculated from Fig. 10; $La_{0.84}Sr_{0.16}MnO_3$; $p_{O_2} = 0.21$ bar; $T = 1000$ °C.

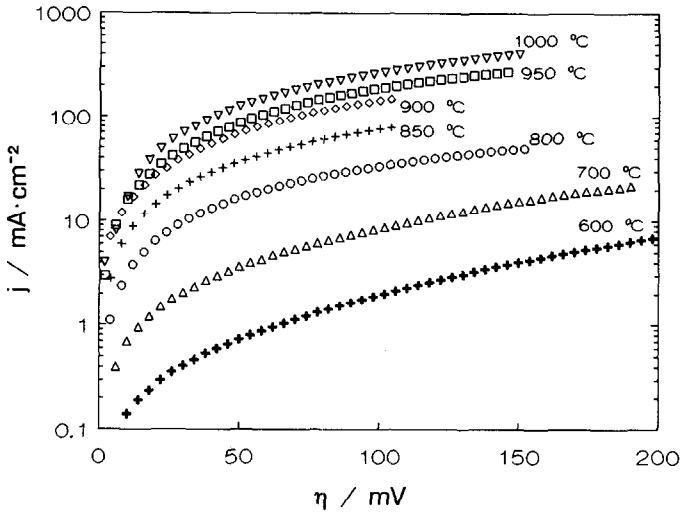

Fig. 12. Tafel plots for the hydrogen oxidation at a Ni–YSZ cermet, $H_2/H_2O = 2/1$ in argon; temperatures as indicated.

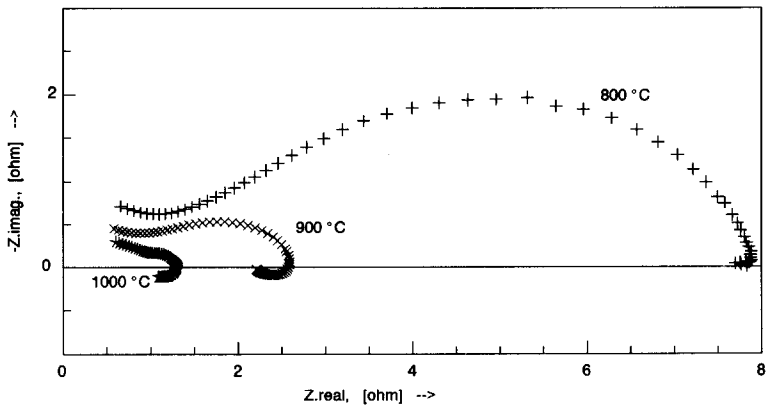

Fig. 13. Impedance spectra for a Ni–YSZ cermet at equilibrium potential in $H_2/H_2O = 2/1$; temperatures as indicated.

spectra for a Ni–YSZ cermet at equilibrium with $H_2/H_2O = 2/1$ in argon (i.e., zero overvoltage) measured at different temperatures are shown in Fig. 13.

At 1000 °C the current density is 270 mA cm^{-2} at an overvoltage of 100 mV. At the same temperature the polarization impedance amounts 0.65 Ω cm^2. With decreasing temperature the polarization impedance increases, as can be seen in Fig. 13. In consequence, the attainable current densities at an overvoltage of 100 mV at lower temperatures reach values below 100 mA cm^{-2}, which makes the Ni–YSZ cermet difficult to use as an anode material in a SOFC operating at reduced temperatures.

To evaluate a reaction mechanism for the hydrogen oxidation at the Ni–YSZ cermet, current-density overvoltage curves and impedance spectra were simulated. The results of the first calculations show that a simple reaction mechanism, involving dissociative adsorption of hydrogen, followed by a charge-transfer of oxygen ions from the electrolyte, is not consistent with the experimental data. It is probable that an additional surface diffusion step, either of hydrogen atoms over the nickel surface or oxygen ions over the electrolyte surface, must be incorporated into the reaction mechanism.

An analysis of the temperature dependence of the current density at constant overvoltage revealed two distinct regions. In the lower temperature region (600–900 °C) activation energies calculated from Arrhenius plots are slightly dependent on the overvoltage and amount to 130 ± 10 kJ mol^{-1}.

Conclusions

As shown above, perovskite cathodes made by WPS show good performance under typical high temperature fuel cell conditions. Nevertheless, the catalytic activity of $La_{0.84}Sr_{0.16}MnO_3$ is low, especially in the high-temperature range $T > 800$ °C, where activation energies are of the order of 200 kJ mol^{-1}. To further improve these cathodes, more fundamental information about the reaction mechanism of the oxygen-exchange reaction is required. The results of the potential and temperature dependence of the reaction, together with the results of the oxygen partial pressure dependence, suggest that a complex reaction mechanism, consisting of several partial reactions, is present.

Together with the results from impedance measurements, we conclude that the overall reaction rate is determined not only by charge transfer, but also by the competition of the charge-transfer step with additional reaction steps such as adsorption of oxygen on to the electrode surface or the surface diffusion of adsorbed oxygen species. The situation is further complicated in that the reaction mechanism appears to change: (i) with temperature (change of both the activation energy and the pre-exponential factor); (ii) with differing oxygen partial pressure, and (iii) with the sintering temperature (change of the composition and geometry of the reaction zone). It is thus not surprising that different reaction mechanisms with different rate-determining steps have been proposed in the literature, depending on the above parameters.

The nickel–zirconia cermet anode fabricated by WPS can be used in SOFC at high temperatures but is less suitable for use at lower temperatures. The determination of a possible reaction mechanism based on experimental data and simulation should give guidelines for improvement of the anodes.

References

1 A. Ruder, H.-P. Buchkremer, H. Jansen, W. Malléner and D. Stöver, *Surf. Coat. Technol., 53* (1992) 71.
2 B. Steffen, J. Divisek, H.G. Baunach and K. Wippermann, in preparation.
3 B.A. Boukamp, Equivalent Circuit, *Internal Rep. CT89/214/128,* University of Twente, 1989.
4 K.J. Vetter, *Z. Elektrochem., 55* (1951) 121.
5 K.J. Vetter, *Z. Elektrochem., 59* (1955) 596.
6 A.J.A. Winnubst, A.H.A. Scharenborg and A.J. Burggraaf, *Solid State Ionics, 14* (1984) 319.
7 B.A. van Hassel, B.A. Boukamp and A.J. Burggraaf, *Solid State Ionics, 48* (1991) 155.
8 A. Kornyshev and K. Wippermann, unpublished results.
9 O. Yamamoto, Y. Takeda, R. Kanno and T. Kojima, *Proc. 1st SOFC Symp., Hollywood, FL, USA, 1989,* p. 242.